

Chirality-Dependent Structural Transformation in Chiral 2D Perovskites under High Pressure

Meng-En Sun,[◆] Yonggang Wang,[◆] Fei Wang, Jiangang Feng, Lingrui Wang, Hanfei Gao, Gaosong Chen,* Jiazhen Gu, Yongping Fu, Kejun Bu, Tonghuan Fu, Junlong Li, Xujie Lü, Lei Jiang, Yuchen Wu,* and Shuang-Quan Zang*



Cite This: *J. Am. Chem. Soc.* 2023, 145, 8908–8916



Read Online

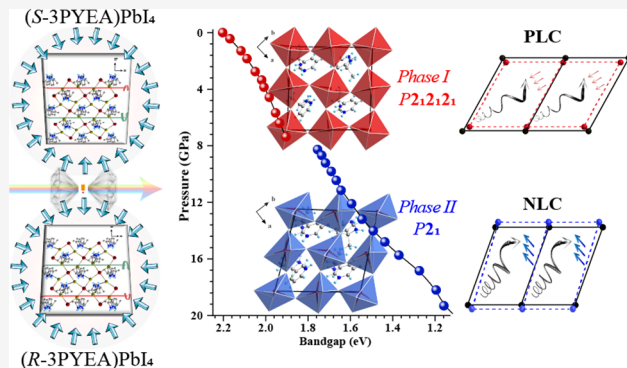
ACCESS |

Metrics & More

Article Recommendations

Supporting Information

ABSTRACT: Chiral perovskites have attracted considerable attention owing to their potential applications in spintronic- and polarization-based optoelectronic devices. However, the structural chirality/asymmetry transfer mechanism between chiral organic ammoniums and achiral inorganic frameworks is still equivocal, especially under extreme conditions, as the systematic structural differences between chiral and achiral perovskites have been rarely explored. Herein, we successfully synthesized a pair of new enantiomeric chiral perovskite (*S/R*-3PYEA) PbI_4 ($3\text{PYEA}^{2+} = \text{C}_5\text{NH}_5\text{C}_2\text{H}_4\text{NH}_3^{2+}$) and an achiral perovskite (*rac*-3PYEA) PbI_4 . Hydrostatic pressure was used, for the first time, to systematically investigate the differences in the structural evolution and optical behavior between (*S/R*-3PYEA) PbI_4 and (*rac*-3PYEA) PbI_4 . At approximately 7.0 GPa, (*S/R*-3PYEA) PbI_4 exhibits a chirality-dependent structural transformation with a bandgap “red jump” and dramatic piezochromism from translucent red to opaque black. Upon further compression, a previously unreported chirality-induced negative linear compressibility (NLC) is achieved in (*S/R*-3PYEA) PbI_4 . High-pressure structural characterizations and first-principles calculations demonstrate that pressure-driven homodirectional tilting of homochiral ammonium cations strengthens the interactions between *S/R*-3PYEA $^{2+}$ and Pb—I frameworks, inducing the formation of new asymmetric hydrogen bonds N—H···I—Pb in (*S/R*-3PYEA) PbI_4 . The enhanced asymmetric H-bonding interactions further break the symmetry of (*S/R*-3PYEA) PbI_4 and trigger a greater degree of in-plane and out-of-plane distortion of $[\text{PbI}_6]^{4-}$ octahedra, which are responsible for chirality-dependent structural phase transition and NLC, respectively. Nevertheless, the balanced H-bonds incurred by equal proportions of S-3PYEA $^{2+}$ and R-3PYEA $^{2+}$ counteract the tilting force, leading to the absence of chirality-dependent structural transition, spectral “red jump”, and NLC in (*rac*-3PYEA) PbI_4 .



INTRODUCTION

Chiral organic–inorganic hybrid halide perovskites (OIHPs), which combine the unique physicochemical features of chiral materials with the excellent optoelectronic and spintronic properties of halide perovskites,^{1,2} are promising candidates for spin modulation,^{3–5} nonlinear optics,^{6–8} bulk photovoltaics,⁹ ferroelectrics,^{10,11} and circularly polarized light (CPL) detectors.^{12–15} Despite the excellent chiral properties achieved in chiral OIHPs, the structural chirality/asymmetry transfer mechanism from chiral organic molecules to achiral inorganic sublattices remains unclear, especially under extreme conditions (i.e., high pressure and low temperature). To fully exploit the great potential of chiral OIHPs, an in-depth understanding of the structure–property relationships of chiral OIHPs is highly demanded. Thus, researchers have recently begun to focus their attention on the correlation between the structures and properties of chiral OIHPs.^{16–21} The structure–property relationships of chiral OIHPs can be regulated by

manipulating the chemical composition to alter the intermolecular interactions of chiral ammoniums and the distortion of inorganic sublattices.^{17–20} Moreover, low-temperature-induced lattice contraction can also tune the structural evolution and optical behavior of chiral OIHPs to a certain extent.²¹ However, the complex chemical synthesis and limited adjustment range of temperature severely hinder insights into the underlying structure–property relationships of chiral OIHPs. Exploring an effective strategy to clarify the origin of the intriguing chiral properties in chiral OIHPs is of great significance.

Received: November 24, 2022

Published: April 14, 2023



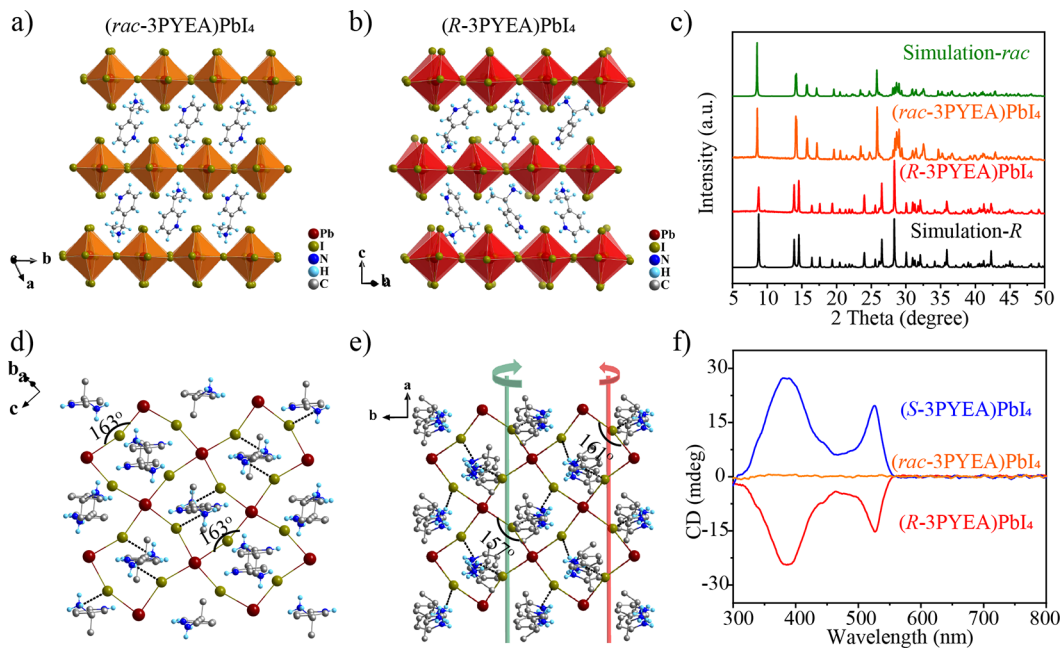


Figure 1. Structural and optical properties of (*S*, *R*, and *rac*-3PYEA)PbI₄ under ambient conditions. Schematic single-crystal X-ray structures of (a) (*rac*-3PYEA)PbI₄ and (b) (*R*-3PYEA)PbI₄. (c) PXRD patterns of (*rac*-3PYEA)PbI₄ and (*R*-3PYEA)PbI₄. (d) (*rac*-3PYEA)PbI₄ shows a single equatorial Pb—I—Pb bond angle of 163° without the out-of-plane distortions of I atoms. (e) In-plane views of Pb—I layers in (*R*-3PYEA)PbI₄ show two different equatorial Pb—I—Pb bond angles of 157 and 161°. The axial I atoms are omitted for clarity. The red and green lines represent the 2₁-screw axes. (f) CD spectra of thin films of (*S*-3PYEA)PbI₄, (*R*-3PYEA)PbI₄, and (*rac*-3PYEA)PbI₄ recorded under ambient conditions.

Hydrostatic pressure, as a physical parameter independent of chemical composition and temperature, is regarded as a powerful and clean tool to study the structure–property relationships of materials that cannot be revealed under ambient conditions.^{22–31} The application of high-pressure on achiral OIHPs has achieved bandgap tunability,^{32–34} enhanced photocurrent,³⁵ improved emission performance,^{36–38} and prolonged carrier lifetime.^{39–41} Nevertheless, the evolution of the crystal structures and properties for chiral OIHPs under high pressure remains unexploited. Owing to unique asymmetric hydrogen bonding interactions between chiral organic ammoniums and achiral inorganic frameworks, pressure-driven structural evolution and optical behavior in chiral OIHPs are expected to be significantly different from the pressure effects in achiral OIHPs. Therefore, extending the hydrostatic pressure effect to chiral OIHPs is vital to reveal the fountainhead and evolution of chiral properties.

In this work, by introducing chiral *S* or *R*-1-(3-pyridyl)-ethanamine and racemic 1-(3-pyridyl)ethanamine into Pb—I frameworks, we successfully prepared two novel Dion–Jacobson (DJ) chiral two-dimensional (2D) OIHPs, (*S*- or *R*-3PYEA)PbI₄ (3PYEA²⁺ = C₅NH₅C₂H₄NH₃²⁺) and an achiral OIHP, (*rac*-3PYEA)PbI₄ (Figure S1). A series of in situ high-pressure experiments, including angle-dispersive synchrotron X-ray diffraction (ADXRD) and Raman, photoluminescence (PL), absorption, and time-resolved PL (TRPL) spectroscopy, were performed to investigate the pressure-induced structural variation and optical behavior of (*S*, *R*, and *rac*-3PYEA)PbI₄. At approximately 7.0 GPa, (*S*/*R*-3PYEA)PbI₄ undergoes a structural phase transition from the orthorhombic phase to the monoclinic phase with a bandgap “red jump” and dramatic piezochromism from translucent red to opaque black. Upon further compression, previously unreported NLC behavior along the *c*-axis direction, perpendicular to the Pb—I inorganic layers of (*S*/*R*-3PYEA)PbI₄, was observed. In situ

high-pressure structural characterizations and density functional theory (DFT) results demonstrate that the new asymmetric hydrogen bonds between *S*/*R*-3PYEA²⁺ and the Pb—I inorganic frameworks, induced by the pressure-driven homodirectional tilting of homochiral amines (*S* or *R*-3PYEA²⁺), are the origin of structural chirality/asymmetry in these chiral perovskites under high pressure. The homodirectional tilting of *S* or *R*-3PYEA²⁺ not only regulates the interlayer spacing of the Pb—I layers but also strengthens asymmetric H-bonding interactions. The enhanced asymmetric H-bonding interactions further break the symmetry of (*S*/*R*-3PYEA)PbI₄ and trigger a greater degree of in-plane and out-of-plane distortion of [PbI₆]⁴⁻ octahedra, which are responsible for chirality-dependent structural phase transition and NLC, respectively. However, equal proportions of *S*-3PYEA²⁺ and *R*-3PYEA²⁺ incur balanced H-bonding interactions between the organic amine cations and Pb—I inorganic layers, leading to the absence of chirality-dependent structural transition, spectral “red jump”, and NLC in (*rac*-3PYEA)PbI₄. Our work not only provides insights into the underlying structural chirality/asymmetry transfer mechanism under high pressure and enriches the physicochemical features of chiral OIHPs but also expands the category of NLC candidate materials.

RESULTS AND DISCUSSION

Single crystals of (*rac*/*S*/*R*-3PYEA)PbI₄ were grown by slowly cooling an aqueous HI solution containing stoichiometric amounts of PbI₂ and *rac*/*S*/*R*-3PYEA. Single-crystal X-ray diffraction (SCXRD) analysis under ambient conditions showed that (*rac*-3PYEA)PbI₄ crystallizes in the centrosymmetric *P*-1 space group, whereas (*S*-3PYEA)PbI₄ and (*R*-3PYEA)PbI₄ adopt the chiral *P*2₁2₁2₁ space group (Tables S1–S3). As shown in Figure 1a,b and Figure S2a, the [PbI₆]⁴⁻

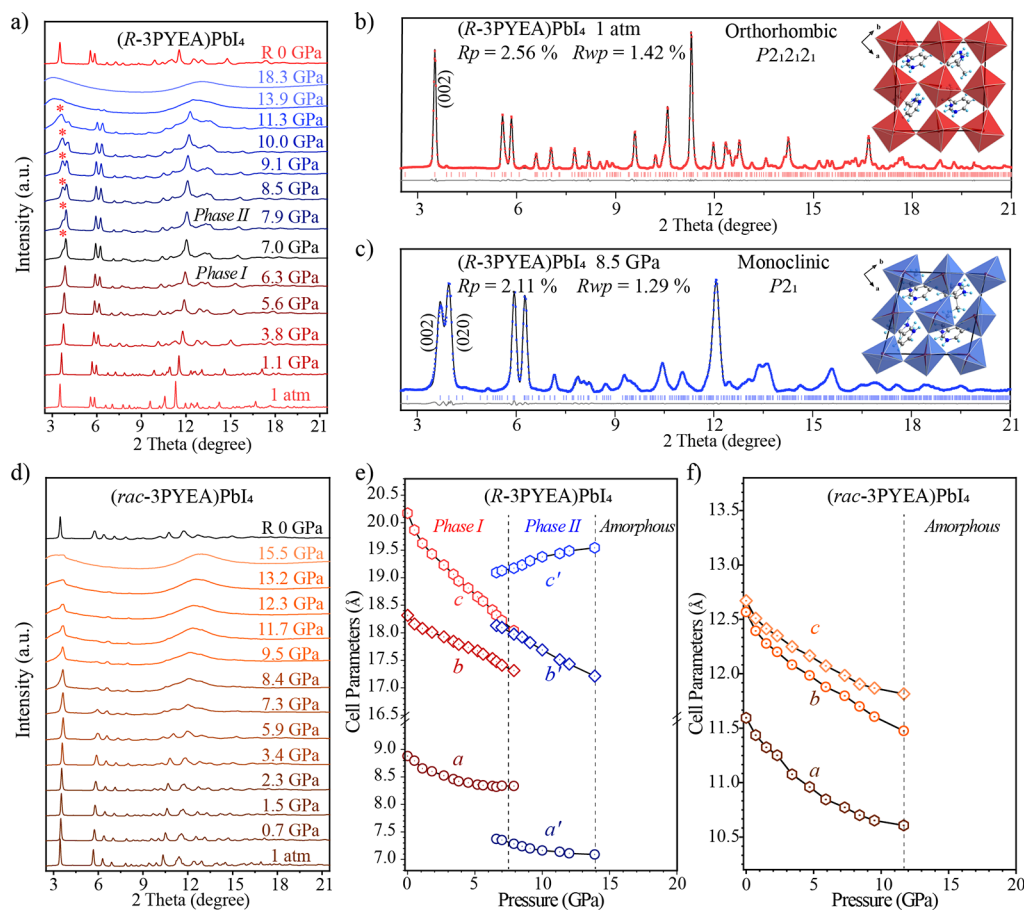


Figure 2. In situ structural characterization of $(R\text{-}3\text{PYEA})\text{PbI}_4$ and $(rac\text{-}3\text{PYEA})\text{PbI}_4$ under high pressure. (a) ADXRD patterns of $(R\text{-}3\text{PYEA})\text{PbI}_4$ at the selected pressure. (b, c) Rietveld refinement results for the ADXRD patterns of $(R\text{-}3\text{PYEA})\text{PbI}_4$ collected at (b) 1 atm and (c) 8.5 GPa. (d) ADXRD patterns of $(rac\text{-}3\text{PYEA})\text{PbI}_4$ at the selected pressure. Pressure-dependence lattice constants of (e) $(R\text{-}3\text{PYEA})\text{PbI}_4$ and (f) $(rac\text{-}3\text{PYEA})\text{PbI}_4$.

octahedra share vertex iodine ions to form a Pb–I layered structure, and the inorganic Pb–I sheets combine with the organic divalent $rac/R\text{-}3\text{PYEA}^{2+}$ cations in the monolayer through Coulomb and hydrogen bonding interactions to form a 2D DJ perovskite phase.^{42–44} The well-overlapped powder X-ray diffraction (PXRD) patterns between the as-synthesized samples and simulated single-crystal data confirm crystal phase purity (**Figure 1c** and **Figure S3**). Comparison of the number of hydrogen bonds in the basic units of chiral ($S/R\text{-}3\text{PYEA})\text{PbI}_4$ and achiral ($rac\text{-}3\text{PYEA})\text{PbI}_4$ and the proportion of H···I interactions around individual organic amines indicates that $(S/R\text{-}3\text{PYEA})\text{PbI}_4$ has stronger hydrogen bonding interactions than $(rac\text{-}3\text{PYEA})\text{PbI}_4$ (**Figure S1d–f**, **Figure S4** and **Tables S4–S6**). The stronger hydrogen bonding interactions and the deeper intrusion of chiral ammonium cations in $(S/R\text{-}3\text{PYEA})\text{PbI}_4$ results in a smaller interlayer spacing (3.36 Å) compared to $(rac\text{-}3\text{PYEA})\text{PbI}_4$ (3.94 Å) (**Figure S5**).

To further evaluate the impact of introducing chiral ammonium cations into the OIHPs, we systematically analyzed the structural distortion of the inorganic Pb–I sheets. As shown in **Figure 1e** and **Figure S2b**, the equatorial bond angle disparity in chiral ($S/R\text{-}3\text{PYEA})\text{PbI}_4$ likely results from the asymmetric hydrogen bonding associated with the in-plane I atoms (**Figure S1h,i**). Such asymmetric hydrogen bonding also incurs out-of-plane distortion for equatorial I atoms, which propagates helically around the 2_1 -screw axis parallel to the a

axis.⁴⁵ However, in $(rac\text{-}3\text{PYEA})\text{PbI}_4$, this type of helical distortion was not observed (**Figure 1d** and **Figure S1g**). As a result, with the introduction of chiral organic cations, chirality can be successfully transferred to the inorganic Pb–I sheets to produce chiral OIHPs. This is further confirmed by the opposite signals of $(S\text{-}3\text{PYEA})\text{PbI}_4$ and $(R\text{-}3\text{PYEA})\text{PbI}_4$ in the circular dichroism (CD) spectra (**Figure 1f** and **Figures S13, S14**). The CD spectra of $(rac/S/R\text{-}3\text{PYEA})\text{PbI}_4$ were obtained based on the prepared thin films with high crystalline phase purity and good crystallinity (**Figures S6–S12**). We have also performed low-frequency Raman measurements on $(rac\text{-}3\text{PYEA})\text{PbI}_4$ and $(R\text{-}3\text{PYEA})\text{PbI}_4$. Distinct low-frequency vibrational modes associated with the inorganic framework can be observed in these two structures due to the different crystal structures and bonding environments (**Figure S15**). By comparing the two spectra, the low-frequency Raman modes of $(R\text{-}3\text{PYEA})\text{PbI}_4$ generally shift to lower frequencies in energy despite the differences in peak intensity. The softened Raman modes of $(R\text{-}3\text{PYEA})\text{PbI}_4$ can be explained by the longer average Pb–I bond length of $(R\text{-}3\text{PYEA})\text{PbI}_4$ (3.23 Å) relative to that of $(rac\text{-}3\text{PYEA})\text{PbI}_4$ (3.21 Å) at ambient conditions. To evaluate the optical properties of $(S/R\text{-}3\text{PYEA})\text{PbI}_4$ and $(rac\text{-}3\text{PYEA})\text{PbI}_4$ under ambient conditions, their UV–visible absorption and PL spectra were collected (**Figure S16**). The chiral and achiral perovskites present an absorption resonance at \sim 530 nm and a sharp PL peak at \sim 540 nm, indicating free exciton emission at ambient conditions. The excitonic bands in

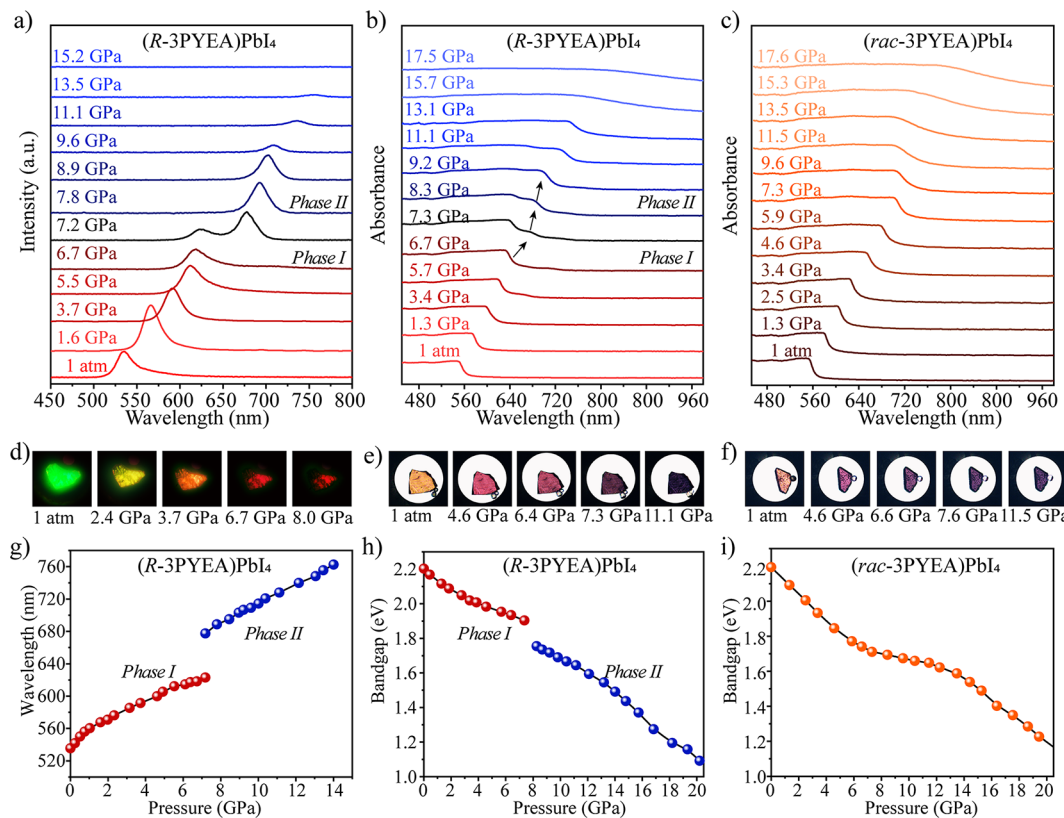


Figure 3. Spectroscopic measurements of $(R\text{-}3\text{PYEA})\text{PbI}_4$ and $(rac\text{-}3\text{PYEA})\text{PbI}_4$ under high pressure. (a) In situ pressure-dependent PL and (b) absorption spectra of $(R\text{-}3\text{PYEA})\text{PbI}_4$ and (c) absorption spectrum of $(rac\text{-}3\text{PYEA})\text{PbI}_4$. Microphotographs in the sample chamber at selected pressures (d) under the ultraviolet field for $(R\text{-}3\text{PYEA})\text{PbI}_4$ and natural light for (e) $(R\text{-}3\text{PYEA})\text{PbI}_4$ and (f) $(rac\text{-}3\text{PYEA})\text{PbI}_4$. (g) Variations of the PL peak of $(R\text{-}3\text{PYEA})\text{PbI}_4$ with pressure. Variations of bandgap values of (h) $(R\text{-}3\text{PYEA})\text{PbI}_4$ and (i) $(rac\text{-}3\text{PYEA})\text{PbI}_4$ with pressure.

$(S/R\text{-}3\text{PYEA})\text{PbI}_4$ are blueshifted by ~ 10 meV relative to $(rac\text{-}3\text{PYEA})\text{PbI}_4$, which is attributed to the longer average Pb—I bond length, smaller Pb—I—Pb band angle, and more pronounced structural distortions in the $(S/R\text{-}3\text{PYEA})\text{PbI}_4$ (Table S7).^{45,46} Additionally, there was no obvious change in PXRD, absorption, and emission spectra within 1 month, indicating good stability of the prepared crystals under ambient conditions (Figures S17–S19).

To further analyze the effect of chirality on the structure of the OIHPs, we collected the pressure-dependent ADXRD and Raman spectra of $(S/R\text{-}3\text{PYEA})\text{PbI}_4$ and $(rac\text{-}3\text{PYEA})\text{PbI}_4$. Ruby spheres were put in the chamber for pressure calibration (Figure S20). As shown in Figure 2a, below 7.0 GPa, all Bragg diffraction peaks shift toward higher diffraction angles upon compression, indicating that pressure-induced lattice shrinkage occurs in the initial phase (phase I, $P_{2\bar{1}}2_12_1$) of $(R\text{-}3\text{PYEA})\text{PbI}_4$ (Figure 2b). Above 7.0 GPa, with the gradual appearance of a new diffraction peak at 3.71° , a structural transition was observed. The new phase (phase II) can be fitted by a monoclinic structure with a space group $P2_1$ (Figure 2c). In phase II, the new diffraction peak shifts toward a lower angle with compression, while the others shifted in the opposite direction. Moreover, the corresponding pressure-dependent d -spacings show a significant expansion along the (002) plane (Figure S21), suggesting that phase II exhibits an anomalous compression behavior under pressure. With further compression to 13.9 GPa, the gradual weakening and broadening of diffraction peaks indicate the beginning of the structural amorphization of phase II. The pressure-dependent ADXRD patterns of $(S\text{-}3\text{PYEA})\text{PbI}_4$ are similar to $(R\text{-}3\text{PYEA})\text{PbI}_4$.

$(S/R\text{-}3\text{PYEA})\text{PbI}_4$ (Figure S22). In contrast, the Bragg diffraction peaks in $(rac\text{-}3\text{PYEA})\text{PbI}_4$ all monotonically shift toward higher angles upon compression and the corresponding interplanar spacings decrease, suggesting that $(rac\text{-}3\text{PYEA})\text{PbI}_4$ undergoes lattice shrinkage with increasing pressure (Figure 2d and Figure S23). These results demonstrate that $(S/R\text{-}3\text{PYEA})\text{PbI}_4$ exhibit chirality-dependent structural transformation and anomalous compression behavior under high pressure.

The chirality-dependent structural transformation is further confirmed by in situ Raman spectroscopy. As shown in Figure S24, the vibrational modes of the inorganic framework reside at low-frequency regions due to the heavy atoms, whereas the Raman modes involving the organic cations reside at the mid- and high-frequency regions. According to the results of the theoretical calculations, the Raman modes of $(rac/R\text{-}3\text{PYEA})\text{PbI}_4$ could be assigned (Tables S8 and S9). The Raman peaks of $(rac\text{-}3\text{PYEA})\text{PbI}_4$ at 51.2 , 83.5 , and 96.9 cm $^{-1}$ are attributed to Pb—I octahedra in-plane scissoring, in-phase Pb—I stretching, and Pb—I symmetric stretching, respectively (Figures S24a and S25). During the comparison, $(R\text{-}3\text{PYEA})\text{PbI}_4$ exhibits four Raman modes in the low-frequency region, i.e., 56.4 , 87.4 , 107.4 , and 159.3 cm $^{-1}$, which are attributed to the Pb—I octahedra in-plane twisting, in-phase Pb—I stretching, Pb—I antisymmetric stretch, and Pb—I octahedra out-of-plane twisting, respectively (Figures S24b and S26). Upon compression, all Raman active modes of $(rac\text{-}3\text{PYEA})\text{PbI}_4$ shift to higher wavenumbers without splitting, as seen in Figures S27 and S28. This further indicates that the achiral OIHP, $(rac\text{-}3\text{PYEA})\text{PbI}_4$, only undergoes lattice shrinkage

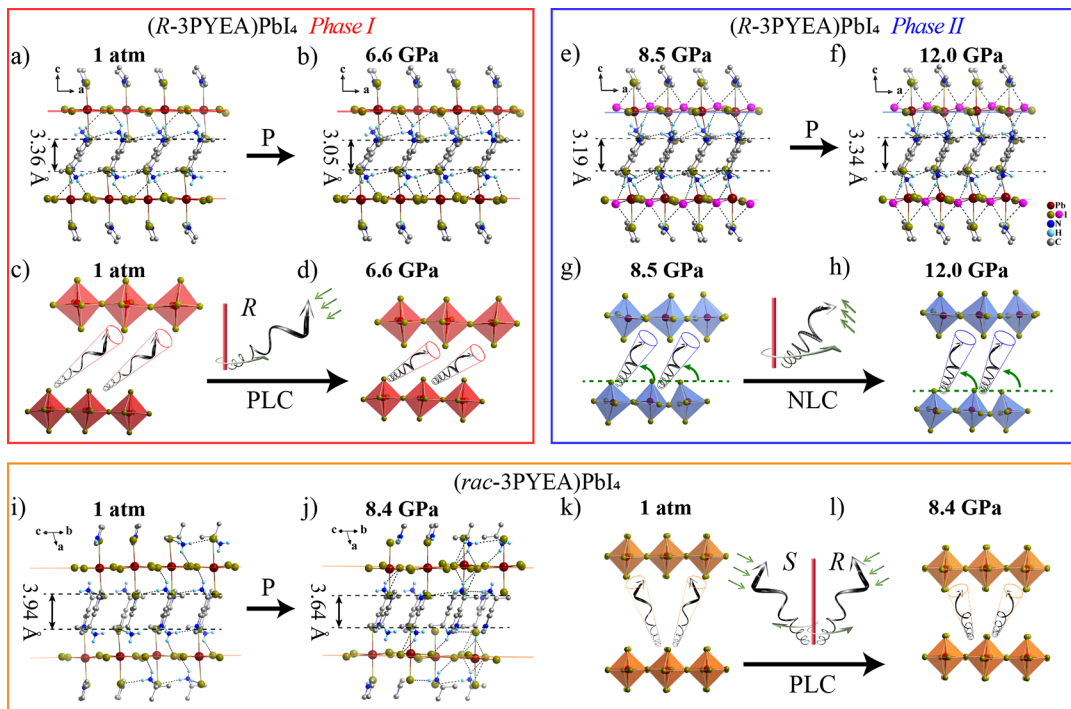


Figure 4. Illustration of the compression process of $(R\text{-}3\text{PYEA})\text{PbI}_4$ and $(rac\text{-}3\text{PYEA})\text{PbI}_4$ under hydrostatic high pressure. Compression behavior in response to the increased pressures and corresponding spring mechanism in (a–d) phase I of $(R\text{-}3\text{PYEA})\text{PbI}_4$, (e–h) phase II of $(R\text{-}3\text{PYEA})\text{PbI}_4$, and (i–l) $(rac\text{-}3\text{PYEA})\text{PbI}_4$. The left and right helix springs denote $S\text{-}3\text{PYEA}^{2+}$ and $R\text{-}3\text{PYEA}^{2+}$, respectively. The green arrow shows the direction of movement for the molecule under compression.

without any structural phase transition within the examined pressure range. Meanwhile, the split and broadened vibrational bands appeared in the pressure-dependent Raman spectra of $(S/R\text{-}3\text{PYEA})\text{PbI}_4$ (Figures S29–S32), further verifying the occurrence of pressure-induced phase transition and amorphization.

The variation of the lattice parameters of $(R\text{-}3\text{PYEA})\text{PbI}_4$ and $(rac\text{-}3\text{PYEA})\text{PbI}_4$ as a function of pressure was plotted to obtain further insights into their pressure-dependent structural evolution (Tables S10,S11). The lattice parameters of $(R\text{-}3\text{PYEA})\text{PbI}_4$ varied discontinuously with pressure (Figure 2e), confirming the occurrence of phase transition. In phase I, the unit cell parameters decrease continuously with increasing pressure. Meanwhile, in phase II, the unit cell parameters c' increase with the compression. During the compression, the unit cell volume of $(R\text{-}3\text{PYEA})\text{PbI}_4$ decreases with increasing pressure (Figure S33). This confirms that chirality-dependent NLC occurs mainly along the c axis (perpendicular to the $\text{Pb}\text{--I}$ layers) in phase II. To date, such a phenomenon in OIHPs has not been reported. The calculated compressibility coefficient of the c axis is $K_c = -3.15 \text{ T Pa}^{-1}$. For $(rac\text{-}3\text{PYEA})\text{PbI}_4$, the lattice parameters and unit cell volume continuously decrease upon compression (Figure 2f and Figure S34). Additionally, the crystal maintains the triclinic structure without undergoing any phase transition, as indicated by the slightly changed lattice angles within the examined pressure range (Figure S35). Among them, the upturn of the lattice angle α in the mid-pressure regime can be attributed to the “two-step” compression process in the 2D perovskites.³² It is worth mentioning that the bulk modulus of $(R\text{-}3\text{PYEA})\text{PbI}_4$ phase II ($B_0 = 72.5 \text{ GPa}$) is larger than $(rac\text{-}3\text{PYEA})\text{PbI}_4$ ($B_0 = 35.1 \text{ GPa}$), indicating that $(R\text{-}3\text{PYEA})\text{PbI}_4$ has better structural stability.³³

To explore the effect of introducing chiral ammonium on the optical properties of OIHPs under compression, in situ high-pressure PL and TRPL spectroscopy were carried out. In contrast to the monotonous redshift of the emission peak for $(rac\text{-}3\text{PYEA})\text{PbI}_4$ before amorphization (Figure S36), a discontinuous redshift with the generation of a new emission in the lower-energy region was observed for $(S/R\text{-}3\text{PYEA})\text{PbI}_4$ in the mixed phase (Figure 3a,g and Figures S37 and S38). Upon further compression, the PL spectra of $(S/R\text{-}3\text{PYEA})\text{PbI}_4$ exhibit a chirality-dependent “red jump” behavior. The Commission Internationale de L’Eclairage (CIE) chromaticity coordinates and a series of optical photographs showed that all three perovskites exhibit a wide response range (from green to red) under pressure (Figure 3d and Figures S36c, S39, and S40).

For the in situ high-pressure TRPL measurements, the emission intensities were collected at the wavelengths of the respective main pressure-dependent steady-static PL peaks. Interpreted as the enhanced electron–phonon scattering due to atomic distortion and displacement,^{47–49} the PL decay rate for all three perovskites increased as the pressure increases, and the average lifetimes show a decreasing trend with pressurization (Figures S41–S43).

To monitor the bandgap evolution, UV–visible absorption measurements were carried out. For $(S/R\text{-}3\text{PYEA})\text{PbI}_4$, the variation of the absorption band with pressure is similar to that of the PL peak energy (Figure 3b and Figures S44 and S45). With the formation of new phases at approximately 7.0 GPa, a new absorption band appears in the low-energy region, accompanied by a sudden change in the color of the crystal from red to black (Figure 3e and Figures S46 and S47). The corresponding bandgap energies of $(S/R\text{-}3\text{PYEA})\text{PbI}_4$ also show a discontinuous “red jump” with increasing pressure

(Figure 3h and Figure S48), while in (*rac*-3PYEA)PbI₄, the bandgap energy is reduced rapidly at first and then slowly with pressure (Figures 3c,i and Figure S49). Correspondingly, the color of the (*rac*-3PYEA)PbI₄ crystal gradually deepens with compression (Figure 3f and Figure S50). It would be useful to control the bandgap without changing the composition of chiral OIHPs, especially for the CPL photodetectors.⁵⁰ The weak absorption of NIR light by chiral OIHPs makes it difficult to directly detect CPL in the NIR region. The redshift of the bandgap, ascribed to the phase transition in chiral OIHP, (*S*/*R*-3PYEA)PbI₄, prompted the narrowing of the total bandgap to 1.49 eV at 14.0 GPa before amorphization. Predictably, (*S*/*R*-3PYEA)PbI₄ could achieve the direct detection of NIR-CPL under high pressure.

To fully understand the mechanism of the chirality-dependent structural and optical behavior, the crystal structures of (*R*-3PYEA)PbI₄ and (*rac*-3PYEA)PbI₄ at different pressures were optimized via DFT. For both perovskites, the states near the conduction band minimum (CBM) mainly consist of Pb-6p states, while the valence band maximum (VBM) consists of I-5p and Pb-6s anti-bonding states (Figures S51–S53). Upon compression, the Pb–I bond interactions strengthen (Figure S54) and the Pb–I electron clouds display significant overlap at high pressure. Hence, the VBM move upward, while the CBM move downward to the Fermi level under compression and the bandgaps gradually decrease.⁵¹ The narrowing of the bandgap during the phase transition in (*R*-3PYEA)PbI₄ is ascribed to the further enhanced overlap of the Pb–I electron clouds due to the bending of the Pb–I bonds (Figure S55), which increases the electronic band dispersion. On the other hand, the bandgap energy of (*rac*-3PYEA)PbI₄ reduced slowly in the mid-pressure regime can be attributed to the slow decrease of the Pb–I bonds in this pressure range.⁵² The calculated pressure-dependent bandgap shown in Figures S56 and S57 is in line with experimental results.

To further reveal the role of chiral ammonium cation in the process of structural evolution, the interlayer *d*-spacing of the Pb–I layers and the distortion of the [PbI₆]^{4−} octahedra at different pressures can be obtained by optimizing the crystal structures. The movement and twist of the inorganic layers, as determined by the structural evolution during compression, can be guided by the organic ammonium cations. These cations are similar to springs imposing a nonzero torque.^{53,54} Owing to the lattice shrinkage dominated by a layer-to-layer approach, the shrinking spring layer prompts the interlayer *d*-spacing of the inorganic layers (defined as the distance between adjacent planes determined by terminal I ions) to decrease (Figure S58). The interlayer *d*-spacing decreases in phase I of (*R*-3PYEA)PbI₄ from 3.36 Å at 1 atm to 3.05 Å at 6.6 GPa (Figure 4a–d and Figure S59a,b) and from 3.94 Å at 1 atm to 3.64 Å at 8.4 GPa in (*rac*-3PYEA)PbI₄ (Figure 4i–l and Figure S60), respectively. However, the lattice contractions caused by the increased pressure further produce more pronounced [PbI₆]^{4−} octahedral distortion in (*R*-3PYEA)PbI₄ (Figures S61 and S62). Compared with the less obvious pressure-dependent structural deformation in (*rac*-3PYEA)-PbI₄, (*R*-3PYEA)PbI₄ with larger initial structural deformation would produce greater structural deformation with pressure until it breaks the structural symmetry.

By comparing the structures of (*R*-3PYEA)PbI₄ at 6.6 GPa and 8.5 GPa, we find that organic ammonium cations with reduced compressibility sank deeper into the inorganic layers.

This causes the pyridine N atoms to form new asymmetric hydrogen bond interactions with the equatorial I atoms of the Pb–I sheets (Figure S63a–b). The enhanced asymmetric hydrogen bonding interactions further break the structural symmetry of inorganic frameworks of (*R*-3PYEA)PbI₄ (Figure S64). We attempted to verify the structural chirality/asymmetric transfer mechanism by chirality spectroscopy (i.e., CPL and CD), but commercial high-pressure chirality spectroscopy instruments are currently unavailable. Furthermore, the increased plane angle between Pb–I sheets and the pyridine ring suggests the reorganized conformation of chiral amine cation during structural transformation (Figures S59 and S65). However, none of these structural changes was clearly observed in (*rac*-3PYEA)PbI₄ (Figures S60 and S65). Simultaneously, the rigidity of the interlayer along the *c* axis is enhanced in phase II for (*R*-3PYEA)PbI₄ due to the enhanced hydrogen bonding. Therefore, the introduction of chiral ammoniums leads to greater structural deformation of [PbI₆]^{4−} octahedra and decreases the interlayer compressibility of the Pb–I sheets during the pressurization process.

A small change in the local structure can have a significant impact on the global structure. Owing to the enhanced interactions between the chiral organic ammonium cations and Pb–I sheets in (*R*-3PYEA)PbI₄, the out-of-plane twisted equatorial I atoms further earn the oblique of the [PbI₆]^{4−} octahedra, which breaks the local structure symmetry (i.e., structural phase transition). With the sharp increase of the Pb…Pb…Pb angle along the *a* axis, the Pb–I sheets with approximately square structures in phase I change into the rhombohedral structure in phase II (Figure S63c–f). The dominant compression behavior also changes from a layer-to-layer approach in phase I to intralayer compression in phase II. Unlike in phase I where the shrinking spring layer prompts a decrease in the interlayer *d*-spacing (Figure 4c,d), in phase II, the same tilting direction of homochiral ammonium cations (*S*- or *R*-3PYEA²⁺) forces the out-of-plane-twisted I atoms to move away from the equatorial plane (Figure 4g,h). This is reflected by the increased interlayer *d*-spacing from 3.19 Å at 8.5 GPa to 3.34 Å at 12.0 GPa (Figure 4e,f and Figure S59c,d). In the *c*-axis direction along the interlayer, the chiral OIHP, (*R*-3PYEA)PbI₄, exhibits positive linear compressibility (PLC) in phase I and NLC in phase II (Figure S66). This is consistent with the decrease in unit cell parameter *c* in phase I and the increase in *c* in phase II with increasing pressure. In (*rac*-3PYEA)PbI₄, equal amounts of *R*- and *S*-type organic ammonium cations produced counteracting interactions (Figure 4k,l), resulting in only shortened springs that exhibit PLC along the interlayer direction (Figure S67).

CONCLUSIONS

In summary, we designed and synthesized two novel 2D DJ chiral OIHPs (*S/R*-3PYEA)PbI₄ with small interlayer spacing. Using hydrostatic pressure to study the structure–property relationships of chiral perovskites, for the first time, we demonstrated several intriguing chirality-dependent behaviors including structural phase transitions, spectral “red jump,” and rare NLC behavior under high pressure in (*S/R*-3PYEA)PbI₄. In situ high-pressure experiments and DFT results demonstrate that the pressure-driven homodirectional tilting of homochiral organic ammonium cations (*S*- or *R*-3PYEA²⁺) not only regulates the interlayer spacing of the Pb–I layers but also strengthens the asymmetric hydrogen bonding between *S*/*R*-3PYEA²⁺ and inorganic Pb–I frameworks. The enhanced

asymmetric hydrogen bonding interactions further break the symmetry of (*S/R*-3PYEA)PbI₄ and trigger a greater degree of in-plane and out-of-plane distortion of [PbI₆]⁴⁻ octahedra, which are responsible for the chirality-dependent structural transition and NLC. Furthermore, the strong NIR absorption of (*S/R*-3PYEA)PbI₄ under high pressure makes them promising candidates for high-performance NIR-CPL photodetectors. Our findings not only provide insights into the underlying structural asymmetry transfer mechanism in chiral perovskites under high pressure but also expand the application fields (NLC and NIR-CPL) of chiral perovskites.

ASSOCIATED CONTENT

Supporting Information

The Supporting Information is available free of charge at <https://pubs.acs.org/doi/10.1021/jacs.2c12527>.

Powder X-ray diffraction, Raman spectra, absorption spectra, emission spectra, photoluminescence lifetime, crystallographic tables, and X-ray crystallographic data ([PDF](#))

Accession Codes

CCDC 2207669–2207671 contain the supplementary crystallographic data for this paper. These data can be obtained free of charge via www.ccdc.cam.ac.uk/data_request/cif, or by emailing data_request@ccdc.cam.ac.uk, or by contacting The Cambridge Crystallographic Data Centre, 12 Union Road, Cambridge CB2 1EZ, UK; fax: +44 1223 336033.

AUTHOR INFORMATION

Corresponding Authors

Gaosong Chen – Henan Key Laboratory of Crystalline Molecular Functional Materials, Henan International Joint Laboratory of Tumor Theranostical Cluster Materials, Green Catalysis Center, and College of Chemistry, Zhengzhou University, Zhengzhou 450001, P. R. China;
Email: chengaosong@zzu.edu.cn

Yuchen Wu – Key Laboratory of Bio-inspired Materials and Interfacial Science, Technical Institute of Physics and Chemistry, Chinese Academy of Sciences, Beijing 100190, P. R. China; orcid.org/0000-0002-3451-7062; Email: wuyuchen@iccas.ac.cn

Shuang-Quan Zang – Henan Key Laboratory of Crystalline Molecular Functional Materials, Henan International Joint Laboratory of Tumor Theranostical Cluster Materials, Green Catalysis Center, and College of Chemistry, Zhengzhou University, Zhengzhou 450001, P. R. China; orcid.org/0000-0002-6728-0559; Email: zangsqqzg@zzu.edu.cn

Authors

Meng-En Sun – Henan Key Laboratory of Crystalline Molecular Functional Materials, Henan International Joint Laboratory of Tumor Theranostical Cluster Materials, Green Catalysis Center, and College of Chemistry, Zhengzhou University, Zhengzhou 450001, P. R. China

Yonggang Wang – School of Materials Science and Engineering, Peking University, Beijing 100871, P. R. China; orcid.org/0000-0003-4816-9182

Fei Wang – Key Laboratory of Material Physics, Ministry of Education, School of Physics and Microelectronics, Zhengzhou University, Zhengzhou 450001, P. R. China; orcid.org/0000-0002-3442-9396

Jiangang Feng – Department of Electrical and Computer Engineering, National University of Singapore, Singapore 117583, Singapore; orcid.org/0000-0002-3696-1386

Lingrui Wang – Key Laboratory of Material Physics, Ministry of Education, School of Physics and Microelectronics, Zhengzhou University, Zhengzhou 450001, P. R. China

Hanfei Gao – Key Laboratory of Bio-inspired Materials and Interfacial Science, Technical Institute of Physics and Chemistry, Chinese Academy of Sciences, Beijing 100190, P. R. China; orcid.org/0000-0001-8419-2780

Jiazhen Gu – Beijing National Laboratory for Molecular Science, College of Chemistry and Molecular Engineering, Peking University, Beijing 100871, P. R. China

Yongping Fu – Beijing National Laboratory for Molecular Science, College of Chemistry and Molecular Engineering, Peking University, Beijing 100871, P. R. China; orcid.org/0000-0003-3362-2474

Kejun Bu – Center for High Pressure Science and Technology Advanced Research (HPSTAR), Shanghai 201203, P. R. China; orcid.org/0000-0002-1466-2764

Tonghuan Fu – Center for High Pressure Science and Technology Advanced Research (HPSTAR), Shanghai 201203, P. R. China

Junlong Li – Beijing Synchrotron Radiation Facility, Institute of High Energy Physics, Chinese Academy of Science, Beijing 100049, P. R. China

Xujie Lü – Center for High Pressure Science and Technology Advanced Research (HPSTAR), Shanghai 201203, P. R. China; orcid.org/0000-0001-8402-7160

Lei Jiang – Key Laboratory of Bio-inspired Materials and Interfacial Science, Technical Institute of Physics and Chemistry, Chinese Academy of Sciences, Beijing 100190, P. R. China; orcid.org/0000-0003-4579-728X

Complete contact information is available at:

<https://pubs.acs.org/10.1021/jacs.2c12527>

Author Contributions

◆ M.-E.S. and Y.W. contributed equally to this study.

Notes

The authors declare no competing financial interest.

The X-ray crystallographic coordinates for structures reported in this article have been deposited at the Cambridge Crystallographic Data Centre (CCDC) under deposition numbers CCDC 2207669 ((rac-3PYEA)PbI₄), 2207670 ((S-3PYEA)PbI₄), and 2207671 ((R-3PYEA)PbI₄).

ACKNOWLEDGMENTS

This work was supported by the National Key R&D Program of China (2021YFA1200301, 2018YFA0704803, and 2018YFA0208502), the National Natural Science Foundation of China (nos. 92061201, 52103238, 52173190, and 21988102), the China Postdoctoral Science Foundation (nos. 2021TQ0289 and 2021M700128), and Zhengzhou University. The *in situ* high-pressure powder XRD were performed at the 4W2HP station in the Beijing Synchrotron Radiation Facility (BSRF) and the BL15U1 station in the Shanghai Synchrotron Radiation Facility (SSRF). We appreciate Dr. Yanchun Li and Dr. Dongliang Yang from the Institute of High Energy Physics of the Chinese Academy of Sciences for their help on the ADXRD measurements at high pressure. The authors thank for the support of parallel high-

performance computing of the National Supercomputing Center in Zhengzhou.

■ REFERENCES

- (1) Long, G. K.; Sabatini, R.; Saidaminov, M. I.; Lakhwani, G.; Rasmita, A.; Liu, X. G.; Sargent, E. H.; Gao, W. B. Chiral-perovskite optoelectronics. *Nat. Rev. Mater.* **2020**, *5*, 423–439.
- (2) Ma, S.; Ahn, J.; Moon, J. Chiral Perovskites for Next-Generation Photonics: From Chirality Transfer to Chiroptical Activity. *Adv. Mater.* **2021**, *33*, No. 2005760.
- (3) Long, G. K.; Jiang, C. Y.; Sabatini, R.; Yang, Z. Y.; Wei, M. Y.; Quan, L. N.; Liang, Q. M.; Rasmita, A.; Askerka, M.; Walters, G.; Gong, X. W.; Xing, J.; Wen, X. L.; Quintero-Bermudez, R.; Yuan, H. F.; Xing, G. C.; Wang, X. R.; Song, D. T.; Voznyy, O.; Zhang, M. T.; Hoogland, S.; Gao, W. B.; Xiong, Q. H.; Sargent, E. H. Spin control in reduced-dimensional chiral perovskites. *Nat. Photonics* **2018**, *12*, 528–533.
- (4) Liu, X. J.; Chanana, A.; Huynh, U.; Xue, F.; Haney, P.; Blair, S.; Jiang, X. M.; Vardeny, Z. V. Circular photogalvanic spectroscopy of Rashba splitting in 2D hybrid organic-inorganic perovskite multiple quantum wells. *Nat. Commun.* **2020**, *11*, 323.
- (5) Kim, Y. H.; Zhai, Y. X.; Lu, H. P.; Pan, X.; Xiao, C. X.; Gaulding, E. A.; Harvey, S. P.; Berry, J. J.; Vardeny, Z. V.; Luther, J. M.; Beard, M. C. Chiral-induced spin selectivity enables a room-temperature spin light-emitting diode. *Science* **2021**, *371*, 1129–1133.
- (6) Yao, L.; Zeng, Z.; Cai, C.; Xu, P.; Gu, H.; Gao, L.; Han, J.; Zhang, X.; Wang, X.; Wang, X.; Pan, A.; Wang, J.; Liang, W.; Liu, S.; Chen, C.; Tang, J. Strong second- and shird-harmonic generation in 1D chiral hybrid bismuth halides. *J. Am. Chem. Soc.* **2021**, *143*, 16095–16104.
- (7) Yuan, C.; Li, X.; Semin, S.; Feng, Y.; Rasing, T.; Xu, J. Chiral lead halide perovskite nanowires for second-order nonlinear optics. *Nano Lett.* **2018**, *18*, 5411–5417.
- (8) Fu, D.; Xin, J.; He, Y.; Wu, S.; Zhang, X.; Zhang, X. M.; Luo, J. Chirality-dependent second-order nonlinear optical effect in 1D organic-inorganic hybrid perovskite bulk single crystal. *Angew. Chem., Int. Ed.* **2021**, *60*, 20021–20026.
- (9) Huang, P. J.; Taniguchi, K.; Miyasaka, H. Bulk photovoltaic effect in a pair of chiral-polar layered perovskite-type lead iodides altered by chirality of organic cations. *J. Am. Chem. Soc.* **2019**, *141*, 14520–14523.
- (10) Yang, C. K.; Chen, W. N.; Ding, Y. T.; Wang, J.; Rao, Y.; Liao, W. Q.; Tang, Y. Y.; Li, P. F.; Wang, Z. X.; Xiong, R. G. The first 2D homochiral lead iodide perovskite ferroelectrics: [R- and S-1-(4-Chlorophenyl)ethylammonium]₂PbI₄. *Adv. Mater.* **2019**, *31*, No. 1808088.
- (11) Gao, J. X.; Zhang, W. Y.; Wu, Z. G.; Zheng, Y. X.; Fu, D. W. Enantiomeric perovskite ferroelectrics with circularly polarized luminescence. *J. Am. Chem. Soc.* **2020**, *142*, 4756–4761.
- (12) Chen, C.; Gao, L.; Gao, W. R.; Ge, C. Y.; Du, X.; Li, Z.; Yang, Y.; Niu, G. D.; Tang, J. Circularly polarized light detection using chiral hybrid perovskite. *Nat. Commun.* **2019**, *10*, 1927.
- (13) Wang, L.; Xue, Y. X.; Cui, M. H.; Huang, Y. M.; Xu, H. Y.; Qin, C. C.; Yang, J.; Dai, H. T.; Yuan, M. J. A chiral reduced-dimension perovskite for an efficient flexible circularly polarized light photodetector. *Angew. Chem., Int. Ed.* **2020**, *59*, 6442–6450.
- (14) Li, D.; Liu, X.; Wu, W.; Peng, Y.; Zhao, S.; Li, L.; Hong, M.; Luo, J. Chiral lead-free hybrid perovskites for self-powered circularly polarized light detection. *Angew. Chem., Int. Ed.* **2021**, *60*, 8415–8418.
- (15) Ishii, A.; Miyasaka, T. Direct detection of circular polarized light in helical 1D perovskite-based photodiode. *Sci. Adv.* **2020**, *6*, No. eabd3274.
- (16) Pietropaolo, A.; Mattoni, A.; Pica, G.; Fortino, M.; Schifino, G.; Grancini, G. Rationalizing the design and implementation of chiral hybrid perovskites. *Chem* **2022**, *8*, 1231–1253.
- (17) Jana, M. K.; Song, R. Y.; Xie, Y.; Zhao, R. D.; Sercel, P. C.; Blum, V.; Mitzi, D. B. Structural descriptor for enhanced spin-splitting in 2D hybrid perovskites. *Nat. Commun.* **2021**, *12*, 4982.
- (18) Jin, K.-H.; Zhang, Y.; Li, K.-J.; Sun, M.-E.; Dong, X.-Y.; Wang, Q.-L.; Zang, S.-Q. Enantiomeric single crystals of linear lead(II) bromide perovskitoids with white circularly polarized emission. *Angew. Chem., Int. Ed.* **2022**, *61*, No. e202205317.
- (19) Ahn, J.; Ma, S.; Kim, J. Y.; Kyhm, J.; Yang, W.; Lim, J. A.; Kotov, N. A.; Moon, J. Chiral 2D organic inorganic hybrid perovskite with circular dichroism tunable over wide wavelength range. *J. Am. Chem. Soc.* **2020**, *142*, 4206–4212.
- (20) Lin, J. T.; Chen, D. G.; Yang, L. S.; Lin, T. C.; Liu, Y. H.; Chao, Y. C.; Chou, P. T.; Chiu, C. W. Tuning the circular dichroism and circular polarized luminescence intensities of chiral 2D hybrid organic-inorganic perovskites through halogenation of the organic ions. *Angew. Chem., Int. Ed.* **2021**, *60*, 21434–21440.
- (21) Ma, J. Q.; Fang, C.; Chen, C.; Jin, L.; Wang, J. Q.; Wang, S.; Tang, J.; Li, D. H. Chiral 2D perovskites with a high degree of circularly polarized photoluminescence. *ACS Nano* **2019**, *13*, 3659–3665.
- (22) Bai, F.; Bian, K.; Huang, X.; Wang, Z.; Fan, H. Pressure induced nanoparticle phase behavior, property, and applications. *Chem. Rev.* **2019**, *119*, 7673–7717.
- (23) Minkov, V. S.; Bud'ko, S. L.; Balakirev, F. F.; Prakapenka, V. B.; Chariton, S.; Husband, R. J.; Liermann, H. P.; Eremets, M. I. Magnetic field screening in hydrogen-rich high-temperature superconductors. *Nat. Commun.* **2022**, *13*, 3194.
- (24) Liu, G.; Kong, L.; Yang, W.; Mao, H.-K. Pressure engineering of photovoltaic perovskites. *Mater. Today* **2019**, *27*, 91–106.
- (25) Zeng, Z.; Wen, J.; Lou, H.; Zhang, X.; Yang, L.; Tan, L.; Cheng, B.; Zuo, X.; Yang, W.; Mao, W. L.; Mao, H. K.; Zeng, Q. Preservation of high-pressure volatiles in nanostructured diamond capsules. *Nature* **2022**, *608*, 513–517.
- (26) Ma, Z. W.; Li, Q.; Luo, J. J.; Li, S. R.; Sui, L. Z.; Zhao, D. L.; Yuan, K. J.; Xiao, G. J.; Tang, J.; Quan, Z. W.; Zou, B. Pressure-driven reverse intersystem crossing: New path toward bright deep-blue emission of lead-free halide double perovskites. *J. Am. Chem. Soc.* **2021**, *143*, 15176–15184.
- (27) Guo, S. H.; Bu, K. J.; Li, J. W.; Hu, Q. Y.; Luo, H.; He, Y. H.; Wu, Y. H.; Zhang, D. Z.; Zhao, Y. S.; Yang, W. G.; Kanatzidis, M. G.; Lu, X. J. Enhanced photocurrent of all-inorganic two-dimensional perovskite Cs₂PbI₂Cl₂ via pressure-regulated excitonic features. *J. Am. Chem. Soc.* **2021**, *143*, 2545–2551.
- (28) Li, Q.; Wang, Y. G.; Pan, W. C.; Yang, W. G.; Zou, B.; Tang, J.; Quan, Z. W. High-pressure band-gap engineering in lead-free Cs₂AgBiBr₆ double perovskite. *Angew. Chem., Int. Ed.* **2017**, *56*, 15969–15973.
- (29) Muscarella, L. A.; Ducinskas, A.; Dankl, M.; Andrzejewski, M.; Casati, N. P. M.; Rothlisberger, U.; Maier, J.; Graetzel, M.; Ehrler, B.; Milic, J. V. Reversible pressure-dependent mechanochromism of Dion-Jacobson and Ruddlesden-Popper layered hybrid perovskites. *Adv. Mater.* **2022**, *34*, No. 2108720.
- (30) Zhao, D.; Xiao, G.; Liu, Z.; Sui, L.; Yuan, K.; Ma, Z.; Zou, B. Harvesting cool daylight in hybrid organic-inorganic halides microtubules through the reservation of pressure-induced emission. *Adv. Mater.* **2021**, *33*, No. 2100323.
- (31) Jing, X.; Zhou, D.; Sun, R.; Zhang, Y.; Li, Y.; Li, X.; Li, Q.; Song, H.; Liu, B. Enhanced photoluminescence and photoresponsiveness of Eu³⁺ ions-doped CsPbCl₃ perovskite quantum dots under high pressure. *Adv. Funct. Mater.* **2021**, *31*, No. 2100930.
- (32) Kong, L. P.; Liu, G.; Gong, J.; Mao, L. L.; Chen, M. T.; Hu, Q. Y.; Lu, X. J.; Yang, W. G.; Kanatzidis, M. G.; Mao, H. K. Highly tunable properties in pressure-treated two-dimensional Dion-Jacobson perovskites. *Proc. Natl. Acad. Sci. U.S.A.* **2020**, *117*, 16121–16126.
- (33) Wang, J.; Wang, L.; Li, Y.; Fu, R.; Feng, Y.; Chang, D.; Yuan, Y.; Gao, H.; Jiang, S.; Wang, F.; Guo, E. J.; Cheng, J.; Wang, K.; Guo, H.; Zou, B. Pressure-induced metallization of lead-free halide double perovskite (NH₄)₂PbI₆. *Adv. Sci.* **2022**, *9*, No. 2203442.
- (34) Jaffe, A.; Lin, Y.; Mao, W. L.; Karunadasa, H. I. Pressure-induced metallization of the halide perovskite (CH₃NH₃)PbI₃. *J. Am. Chem. Soc.* **2017**, *139*, 4330–4333.

- (35) Lü, X.; Wang, Y.; Stoumpos, C. C.; Hu, Q.; Guo, X.; Chen, H.; Yang, L.; Smith, J. S.; Yang, W.; Zhao, Y.; Xu, H.; Kanatzidis, M. G.; Jia, Q. Enhanced structural stability and photo responsiveness of $\text{CH}_3\text{NH}_3\text{SnI}_3$ perovskite via pressure-induced amorphization and recrystallization. *Adv. Mater.* **2016**, *28*, 8663–8668.
- (36) Shi, Y.; Ma, Z. W.; Zhao, D. L.; Chen, Y. P.; Cao, Y.; Wang, K.; Xiao, G. J.; Zou, B. Pressure-induced emission (PIE) of one-dimensional organic tin bromide perovskites. *J. Am. Chem. Soc.* **2019**, *141*, 6504–6508.
- (37) Sun, M. E.; Geng, T.; Yong, X.; Lu, S. Y.; Ai, L.; Xiao, G. J.; Cai, J. M.; Zou, B.; Zang, S. Q. Pressure-triggered blue emission of zero-dimensional organic bismuth bromide perovskite. *Adv. Sci.* **2021**, *8*, 2004853.
- (38) Guo, S. H.; Zhao, Y. S.; Bu, K. J.; Fu, Y. P.; Luo, H.; Chen, M. T.; Hautzinger, M. P.; Wang, Y. Q.; Jin, S.; Yang, W. G.; Lü, X. J. Pressure-suppressed carrier trapping leads to enhanced emission in two-dimensional perovskite $(\text{HA})_2(\text{GA})\text{Pb}_2\text{I}_7$. *Angew. Chem., Int. Ed.* **2020**, *59*, 17533–17539.
- (39) Liu, G.; Kong, L. P.; Gong, J.; Yang, W. G.; Mao, H. K.; Hu, Q. Y.; Liu, Z. X.; Schaller, R. D.; Zhang, D. Z.; Xu, T. Pressure-induced bandgap optimization in lead-based perovskites with prolonged carrier lifetime and ambient retainability. *Adv. Funct. Mater.* **2017**, *27*, No. 1604208.
- (40) Yuan, Y.; Liu, X. F.; Ma, X.; Wang, X.; Li, X.; Xiao, J.; Li, X.; Zhang, H. L.; Wang, L. Large band gap narrowing and prolonged carrier lifetime of $(\text{C}_4\text{H}_9\text{NH}_3)_2\text{PbI}_4$ under high pressure. *Adv. Sci.* **2019**, *6*, No. 1900240.
- (41) Yin, Y.; Tian, W.; Luo, H.; Gao, Y.; Zhao, T.; Zhao, C.; Leng, J.; Sun, Q.; Tang, J.; Wang, P.; Li, Q.; Lü, X.; Bian, J.; Jin, S. Excellent carrier transport property of hybrid perovskites sustained under high pressures. *ACS Energy Lett.* **2022**, *7*, 154–161.
- (42) Li, X. T.; Hoffman, J. M.; Kanatzidis, M. G. The 2D halide perovskite rulebook: How the spacer influences everything from the structure to optoelectronic device efficiency. *Chem. Rev.* **2021**, *121*, 2230–2291.
- (43) Li, X. T.; Ke, W. J.; Traore, B.; Guo, P. J.; Hadar, I.; Kepenekian, M.; Even, J.; Katan, C.; Stoumpos, C. C.; Schaller, R. D.; Kanatzidis, M. G. Two-dimensional Dion-Jacobson hybrid lead iodide perovskites with aromatic diammonium cations. *J. Am. Chem. Soc.* **2019**, *141*, 12880–12890.
- (44) Mao, L. L.; Ke, W. J.; Pedesseau, L.; Wu, Y. L.; Katan, C.; Even, J.; Wasielewski, M. R.; Stoumpos, C. C.; Kanatzidis, M. G. Hybrid Dion-Jacobson 2D lead iodide perovskites. *J. Am. Chem. Soc.* **2018**, *140*, 3775–3783.
- (45) Jana, M. K.; Song, R. Y.; Liu, H. L.; Khanal, D. R.; Janke, S. M.; Zhao, R. D.; Liu, C.; Vardeny, Z. V.; Blum, V.; Mitzi, D. B. Organic-to-inorganic structural chirality transfer in a 2D hybrid perovskite and impact on Rashba-Dresselhaus spin-orbit coupling. *Nat. Commun.* **2020**, *11*, 4699.
- (46) Du, K. Z.; Tu, Q.; Zhang, X.; Han, Q.; Liu, J.; Zauscher, S.; Mitzi, D. B. Two-Dimensional Lead(II) Halide-Based Hybrid Perovskites Tempered by Acene Alkylamines: Crystal Structures, Optical Properties, and Piezoelectricity. *Inorg. Chem.* **2017**, *56*, 9291–9302.
- (47) Liu, G.; Kong, L. P.; Guo, P. J.; Stoumpos, C. C.; Hu, Q. Y.; Liu, Z. X.; Cai, Z. H.; Gosztola, D. J.; Mao, H. K.; Kanatzidis, M. G.; Schaller, R. D. Two regimes of bandgap red shift and partial ambient retention in pressure-treated two-dimensional perovskites. *ACS Energy Lett.* **2017**, *2*, 2518–2524.
- (48) Wang, Y. Q.; Guo, S. H.; Luo, H.; Zhou, C. K.; Lin, H. R.; Ma, X. D.; Hu, Q. Y.; Du, M. H.; Ma, B. W.; Yang, W. G.; Lü, X. J. Reaching 90% photoluminescence quantum yield in one-dimensional metal halide $\text{C}_4\text{N}_2\text{H}_{14}\text{PbBr}_4$ by pressure-suppressed nonradiative Loss. *J. Am. Chem. Soc.* **2020**, *142*, 16001–16006.
- (49) Yin, T.; Liu, B.; Yan, J.; Fang, Y.; Chen, M.; Chong, W. K.; Jiang, S.; Kuo, J. L.; Fang, J.; Liang, P.; Wei, S.; Loh, K. P.; Sum, T. C.; White, T. J.; Shen, Z. X. Pressure-engineered structural and optical properties of two-dimensional $(\text{C}_4\text{H}_9\text{NH}_3)_2\text{PbI}_4$ perovskite exfoliated nm-thin flakes. *J. Am. Chem. Soc.* **2019**, *141*, 1235–1241.
- (50) Peng, Y.; Liu, X. T.; Li, L. N.; Yao, Y. P.; Ye, H.; Shang, X. Y.; Chen, X. Y.; Luo, J. H. Realization of vis-NIR dual-modal circularly polarized light detection in chiral perovskite bulk crystals. *J. Am. Chem. Soc.* **2021**, *143*, 14077–14082.
- (51) Liu, S.; Sun, S. S.; Gan, C. K.; del Aguila, A. G.; Fang, Y. N.; Xing, J.; Do, T. T. H.; White, T. J.; Li, H. G.; Huang, W.; Xiong, Q. H. Manipulating efficient light emission in two-dimensional perovskite crystals by pressure-induced anisotropic deformation. *Sci. Adv.* **2019**, *5*, No. eaav9445.
- (52) Liu, G.; Gong, J.; Kong, L. P.; Schaller, R. D.; Hu, Q. Y.; Liu, Z. X.; Yan, S.; Yang, W. G.; Stoumpos, C. C.; Kanatzidis, M. G.; Mao, H. K.; Xu, T. Isothermal pressure-derived metastable states in 2D hybrid perovskites showing enduring bandgap narrowing. *Proc. Natl. Acad. Sci. U.S.A.* **2018**, *115*, 8076–8081.
- (53) Szafranski, M. Large negative linear compressibility triggered by hydrogen bonding. *J. Phys. Chem. C* **2020**, *124*, 11631–11638.
- (54) Zhao, Y.; Fan, C. Z.; Pei, C. Y.; Geng, X.; Xing, G. L.; Ben, T.; Qiu, S. L. Colossal negative linear compressibility in porous organic salts. *J. Am. Chem. Soc.* **2020**, *142*, 3593–3599.

□ Recommended by ACS

Chiral Cation Doping for Modulating Structural Symmetry of 2D Perovskites

Yi Xie, David B. Mitzi, et al.

AUGUST 02, 2023

JOURNAL OF THE AMERICAN CHEMICAL SOCIETY

READ ▶

Uncovering Multiple Intrinsic Chiral Phases in $(\text{PEA})_2\text{PbI}_4$ Halide Perovskites

Shahar Zuri, Efrat Lifshitz, et al.

MAY 18, 2023

THE JOURNAL OF PHYSICAL CHEMISTRY LETTERS

READ ▶

Smart Reversible Transformations between Chiral Superstructures of Copper Clusters for Optical and Chiroptical Switching

Zhen Han, Shuang-Quan Zang, et al.

MARCH 13, 2023

JOURNAL OF THE AMERICAN CHEMICAL SOCIETY

READ ▶

Chiral Hybrid Perovskites $(R-/S\text{-CLPEA})_4\text{Bi}_2\text{I}_{10}$ with Enhanced Chirality and Spin–Orbit Coupling Splitting for Strong Nonlinear Optical Circular Dichroism and Spin Se...

Jinjin Zhao, Lei Kang, et al.

JUNE 02, 2023

CHEMISTRY OF MATERIALS

READ ▶

Get More Suggestions >